

# The high-resolution absorption spectroscopy branch on the VUV beamline DESIRS at SOLEIL

Nelson de Oliveira,\* Denis Joyeux, Mourad Roudjane,‡ Jean-François Gil, Bertrand Pilette,§ Lucy Archer, Kenji Ito and Laurent Nahon

Ligne DESIRS, Synchrotron Soleil, L'Orme des Merisiers, Saint-Aubin, BP 48, 91192 Gif-sur-Yvette Cedex, France.

\*Correspondence e-mail: nelson.de.oliveira@synchrotron-soleil.fr

Received 23 March 2016

Accepted 12 April 2016

Edited by S. Svensson, Uppsala University, Sweden

‡ Current address: Department of Physics, Saint Francis Xavier University, PO Box 5000, NS, B2G 2W5, Antigonish, Canada.

§ Current address: Université Paris Sud, Rue du Chateau, Orsay 91400, France.

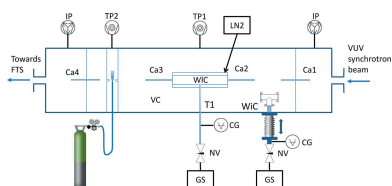
**Keywords:** VUV beamline; Fourier spectroscopy; absorption spectroscopy; high spectral resolution.

A VUV absorption spectroscopy facility designed for ultra-high spectral resolution is in operation as a dedicated branch on the DESIRS beamline at Synchrotron SOLEIL. This branch includes a unique VUV Fourier transform spectrometer (FTS) and a dedicated versatile gas sample chamber. The FTS instrument can cover a large UV–VUV spectral range from 4 to 30 eV, with an ultimate line width of  $0.08\text{ cm}^{-1}$  on a large spectral window,  $\Delta E/E = 7\%$ , over which all spectral features can be acquired in a multiplex way. The performance can be considered to be a middle ground between broadband moderate-resolution spectrometers based on gratings and ultra-high-spectral-resolution VUV tunable-laser-based techniques over very narrow spectral windows. The various available gaseous-sample-handling setups, which function over a wide range of pressures and temperatures, and the acquisition methodology are described. A selection of experimental results illustrates the performance and limitations of the FTS-based facility.

## 1. Introduction

Absorption spectroscopy in the gas phase provides an essential source of information on the position of molecular levels and their couplings, leading in some cases to understanding molecular dynamics. It can also be a powerful analytical technique to access the nature and abundance of species encountered in various environments such as the interstellar medium, planetary and terrestrial atmospheres or plasmas. In this context, establishing accurate wavelength, oscillator strength and isotope shifts over a large spectral domain is a crucial task for understanding the various processes involved in such environments. In this sense, laboratory experiments and theory are both essential to build up large models which are able to give accurate predictions. When electronic transitions are involved, the situation is quite challenging due to the inherent difficulty in carrying out experimental work in the UV and VUV spectral regions, which require in general high-vacuum conditions, and the lack or limitations of available transmitting optics.

Major improvements have been made in recent years in our ability to probe this spectral region with the availability of tunable VUV laser sources (Rupper & Merkt, 2004; Ubachs, 2005) which gave access to unprecedented resolving power ( $\sigma/\delta\sigma > 1 \times 10^7$ ) and wavenumber accuracy ( $\Delta\sigma/\sigma$  as low as  $6 \times 10^{-9}$ ) but have difficulties at quickly covering a large spectral window (Seiler *et al.*, 2005; Trickl *et al.*, 2007). Therefore, in practice, laser-based techniques are generally devoted to narrow-spectral-range experiments associated with ultrahigh resolution. It is worth mentioning recent progress in



the production of VUV and XUV frequency combs, as in the near future this technology will probably make it possible to efficiently cover the far VUV and XUV spectral regions for ultrahigh-precision metrology applications (Kandula *et al.*, 2010; Cingöz *et al.*, 2012).

Fourier transform (FT) spectroscopy is a standard technique covering a broad spectral range spanning from the far infrared down to the near VUV, and dedicated to absorption or emission spectroscopy. The performance of FT spectroscopy (high accuracy of the spectral scale, high resolving power and high efficiency of photon collection) has made this technique popular not only for laboratory analysis but also as a powerful research tool in astrophysics, sometimes used on ground telescopes or deployed in astronomical satellites. FT spectroscopy is in general associated with laboratory sources such as blackbody or gas discharge lamps; nevertheless, high-brilliance sources like those provided by synchrotron facilities can dramatically improve the performance of such instruments in terms of detection sensitivity and signal-to-noise ratio (SNR). This is particularly the case in the mid-infrared and far-infrared regions where most of the facilities exploit the low energy range by coupling commercial Fourier transform spectrometers (FTSs) to synchrotron sources on dedicated beamlines for high-resolution absorption spectroscopy applications (Lerch *et al.*, 2012).

In the higher energy range, VUV absorption spectroscopy is performed using robust and versatile grating-based monochromators. This is the situation of the following non-exhaustive list of beamlines: UV1 on ASTRID/ASTRID2 (Eden *et al.*, 2006), BL03 at NSRRC (Hsieh *et al.*, 1998), VUV BL at Indus-1 (Singh *et al.*, 2011) and of the BESSY II U125 undulator beamline (Reichardt *et al.*, 2001). In general, the spectral resolution depends on the grating optical quality through slope errors, making the manufacture of high-spectral-resolution spectrometers a difficult task in this spectral range. In the VUV, state-of-the-art grating-based monochromators can barely reach a resolving power of  $2 \times 10^5$  (Nahon *et al.*, 2001), with generally diminishing performance with energy. Note that high spectral resolution is required not only to facilitate the analysis of complex spectra but also to measure accurate photoabsorption cross sections. The idea of providing ultra-high spectral resolution combined with a broad spectral coverage in the VUV was the main motivation for the development of a FT spectroscopy branch on the DESIRS beamline over the past years.

DESIRS is a gas-phase undulator-based UV–VUV beamline at Synchrotron SOLEIL and has been designed to address a large number of issues linked to gas-phase spectroscopy and photodynamics (Nahon *et al.*, 2012; see also <http://www.synchrotron-soleil.fr/Recherche/LignesLumiere/DESIRS>). A dedicated branch of the DESIRS beamline was designed to combine a unique VUV FTS and a dedicated multi-purpose gas sample chamber. The VUV FTS has been developed specifically to cover the VUV range where the usual established techniques make use of all-reflective grating-based monochromators to record photoabsorption spectra of molecules. Up to now, a major difficulty for the extension of Fourier

spectroscopy into the far VUV was the strong photoabsorption of materials, making the manufacturing of the beam splitters required for an interferometric device extremely difficult. In order to circumvent this difficulty, the VUV FTS is based on a wavefront-division interferometer, thus allowing for the first time the extension of FT spectroscopy into the far VUV (de Oliveira *et al.*, 2009, 2011).

In this report, we describe the whole FTS branch including the various sample environments (supersonic jet, absorption cells) as well as the specific procedures used in the FTS data reduction, in addition to a detailed error analysis leading to typical accuracy for absolute photoabsorption measurements.

## 2. The VUV FTS photoabsorption branch on the DESIRS beamline

### 2.1. Overall implementation

DESIRS is an undulator-based VUV beamline (Nahon *et al.*, 2012) on the 2.75 GeV storage ring SOLEIL optimized for gas-phase studies of molecular and electronic structures, reactivity and polarization-dependent photodynamics on model or actual systems encountered in the universe, atmosphere and biosphere. It is equipped with a state-of-the-art monochromator for high resolution in the VUV, which feeds into two experimental branches; one branch includes a dedicated electron/ion imaging coincidence spectrometer (Garcia *et al.*, 2013) installed on a molecular beam chamber (Tang *et al.*, 2015) and the other can be connected to various experimental chambers from external users. The FTS branch (Fig. 1) is located upstream of the monochromator and its pre-focusing optics in order to exploit the full spectral bandwidth of the incident undulator ‘pink’ beam. The DESIRS undulator source (HU640) has been designed to offer high flux and variable polarization in the UV–VUV range, between 4 and 40 eV (Marcouille *et al.*, 2007). The undulator radiation is reflected by a pair of mirrors (M1M2) inside the first optical chamber of the beamline. M1 is a cryo-cooled plane mirror that removes most of the heat from the incident beam; M2 is a toroidal mirror that focuses the beam into a dedicated gas-filter chamber and removes the high harmonics from the undulator radiation. An optical aperture adjustment chamber follows, involving four independent blades that allow the source size to be tailored at this location. Downstream, a switchable Si toroidal mirror (MTF) can be inserted to deflect the beam at a 70° incidence angle towards the FTS branch. The beam is always deflected in the horizontal plane in this section of the DESIRS beamline. The MTF mirror focuses the incident beam in the vertical plane onto a 400 μm horizontal entrance slit located 2.4 m downstream of the MTF mirror. The gas sample environmental chamber, described in detail in the next section, is located between the MTF mirror and the FTS entrance slit. The beam is then reflected and split by the scanning wavefront division interferometer, which is based on two roof-shaped mirrors, where it undergoes two reflections at 45° onto SiC-coated reflectors (de Oliveira *et al.*, 2011). Note that the interferometer reflectivity is quite constant in the

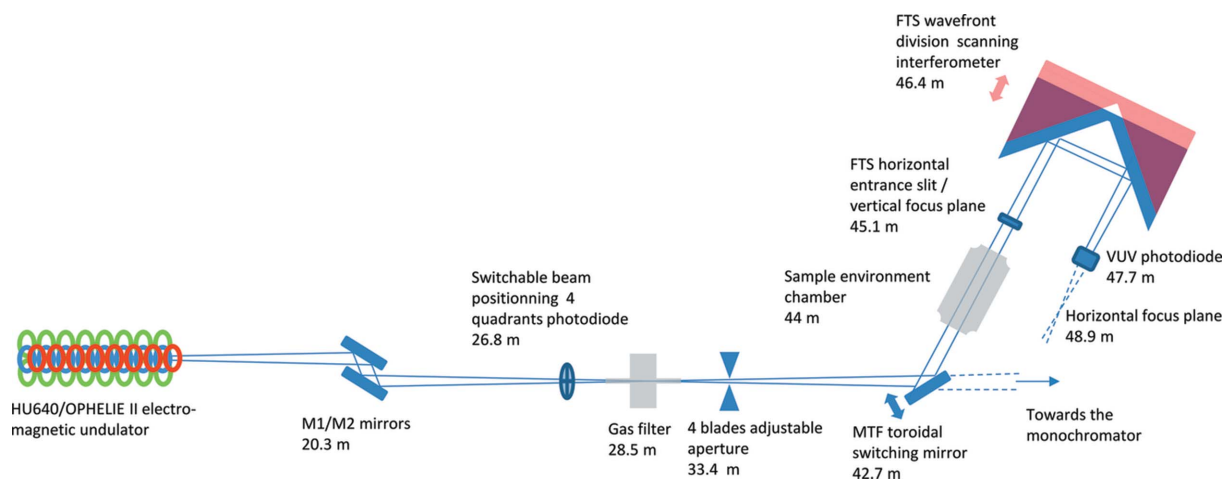


**Figure 1** Schematic layout of the DESIRS beamline feeding the FTS branch (bird's-eye view). The position of the important components is specified in metres from the source. The figure is not drawn to scale.

**Table 1**  
Main performances of the FTS branch.

Spectral window of a single spectrum	Energy range	Minimal spectral resolution	Typical integration time for a single spectrum
$\Delta\sigma/\sigma = 7\%$	4–40 eV	$\delta\sigma = 0.08 \text{ cm}^{-1}$	$20 < t < 3600 \text{ s}^\dagger$

$^\dagger$  Depending on the required resolution and SNR.

range 6–40 eV, about 40%, but is less regular and drops down in the mid-/near-UV range.

## 2.2. Energy range and overall performances

The undulator source polarization can be controlled over the whole spectral range of the beamline. The condition for optimal flux through the FTS is linear vertical polarization of the incident light, as the plane of incidence is horizontal for all the optical elements between the source and the FTS detector. However, linear vertical polarization is limited to the range 6.2–40 eV on the DESIRS beamline, so extension into the UV down to 4 eV is only possible by adding a small amount of horizontal polarization to the vertical one leading to slightly elliptical polarization and therefore to a small loss of photon flux (see §5.2).

The VUV FTS properties and performance have been described in detail previously (de Oliveira *et al.*, 2011). Basically, the FTS is used to provide ultra-high spectral resolution in a broad VUV spectral range, over which an ultimate resolving power close to  $1 \times 10^6$  was demonstrated experimentally and a line width of  $0.2 \text{ cm}^{-1}$  is routinely used by a broad user community (Salumbides *et al.*, 2012; Stark *et al.*, 2014). A review of the performance of the FTS is given in Table 1.

## 2.3. Carbon-contamination effects and cleaning strategies

The MTF mirror horizontal focusing properties have been selected to adjust the size of the beam to the lateral dimension of the VUV FTS photodiode (AXUV from IRD). In practice,

the horizontal focal point stands 1 m downstream of the photodiode in order to reduce the photon density incident on the reflectors of the wavefront division VUV interferometer, reducing the likelihood of carbon contamination. Indeed, the residual vacuum pressure inside the ultra-high-vacuum (UHV) chambers (a few  $10^{-9}$  mbar) and the high-energy photon density incident on the optics ( $\sim 10^{16}$  photons  $\text{s}^{-1}$  at the FT reflector level) are the two main parameters that affect the rate of carbon contamination of the optics leading to a drop of the signal over time (Hollenshead & Klebanoff, 2006).

While the build-up of a carbon layer on the optics of synchrotron soft X-ray beamlines is a well documented problem especially on modern third-generation facilities, such an issue on VUV beamlines has been much less reported. However, since the opening of DESIRS in 2008, a loss of transmitted flux has been observed over time, and different *in situ* and *ex situ* techniques have been employed to clean the optical surfaces and recover the initial flux (Yao-Leclerc *et al.*, 2011; Nahon *et al.*, 2013). On the FTS branch an *in situ* cleaning process is preferred, due to the difficulty and the time needed to properly align the VUV interferometer after an *ex situ* cleaning of the reflectors. We decided to implement a variant of the usual technique consisting in general of using a laboratory UV lamp in order to produce ozone from a high pressure of oxygen and remove the carbon layer from contaminated optics. For implementation in the FTS case, we isolate the FTS chamber from the UHV section of the DESIRS beamline with a  $\text{MgF}_2$  window valve. Then a low pressure of pure  $\text{O}_2$  (a few mbars) is introduced and the undulator, set to a central energy of 8 eV, is directly used as a source for the *in situ* production of reactive ozone molecules and  $\text{O}^*$  radicals. The transmitted flux is monitored by the FTS photodiode and, after a few hours of this treatment, the original signal level is recovered. In practice, this low-pressure method does not require any baking of the chamber, which is a major advantage in our case as most of the interferometer optical blocks are precisely glued together and would not stand a high increase in temperature. Besides, the cleaning is

**Table 2**  
Gas sample environments characteristics.

Setup	Maximum column density <sup>†</sup>	Minimum detectable cross section <sup>†</sup>	Temperature range
Windowless cell	$\sim 7 \times 10^{17} \text{ cm}^{-2}$	$\sim 1.5 \times 10^{-19} \text{ cm}^2$	1000 K down to LN <sub>2</sub> temperature
Free molecular jet	$\sim 2 \times 10^{16} \text{ cm}^{-2}$	$\sim 3 \times 10^{-18} \text{ cm}^2$	Rotational temperature <sup>‡</sup> $\simeq 40\text{--}10$ K
Windowed cells (MgF <sub>2</sub> or LiF windows of various lengths) <sup>§</sup>	$\sim 10^{22} \text{ cm}^{-2}$	$\sim 7 \times 10^{-24} \text{ cm}^2$	Room temperature

<sup>†</sup> See text for details. <sup>‡</sup> Lowest temperature observed on <sup>12</sup>C<sup>16</sup>O: 12 K (Niu *et al.*, 2013). <sup>§</sup> Figures are for the longest available cell (40 cm) under 1 bar.

carried out locally on all of the potentially contaminated surfaces (reflectors and photodiode), preventing a possible oxidation of the metallic parts inside the chamber. Usually, the initial working pressure in the FTS chamber (a few  $10^{-9}$  mbar) is recovered after one or two weeks, matching the typical duration of technical breaks in a synchrotron facility. Note that the increase in SNR was especially spectacular after the first cleaning session, *i.e.* a factor of 20. This cleaning procedure is now performed routinely, approximately every 18 months.

### 3. Gas sample environment

Gas-phase absorption experiments in the VUV are made possible by the use of dedicated gas sample environments. The chamber developed for the FTS branch offers different setups in order to reproduce conditions encountered in natural environments in terms of temperature or pressure, such as a cooled or heated windowless cell, windowed cells of various lengths, or a supersonic jet (see summary in Table 2). In all cases, in contrast with equivalent setups operating in the IR or visible, the absorption is achieved with single-pass cells because of the poor reflectivity of mirrors in a broad VUV range. Nevertheless, absorption cross sections in the VUV are such that, in general, single pass is fine in order to obtain a sufficient column density.

A schematic of the gas sample cell system is shown in Fig. 2. The vacuum chamber consists of a double differential pumping system connected to the MTF chamber upstream and the VUV FTS chamber downstream; both of these chambers are in UHV. If the chamber has to be isolated from the rest of the beamline and vented, the vacuum can be recovered after two hours of pumping time. In the central chamber, pumped by a  $1500 \text{ l s}^{-1}$  turbo pump, three different setups, summarized in Table 2, are available and can be operated independently by the users without breaking the vacuum: a VUV windowed cell, a windowless cell and a supersonic molecular beam, whose chamber is isolated from the main vacuum system by an extra stage of differential pumping. Two different windowless cells are available: one that can be cooled down with a constant flow of liquid nitrogen (LN<sub>2</sub>) and one that can be heated up to a maximum temperature of 1000 K. In addition, a variety of lengths of windowed cells can be used so as to adapt the experimental conditions to the gas sample being analyzed. Therefore, different conditions in terms of temperature and column density can be addressed by the various setups.

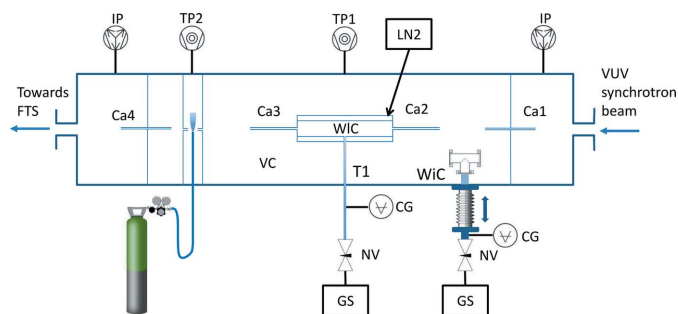


**Figure 2**

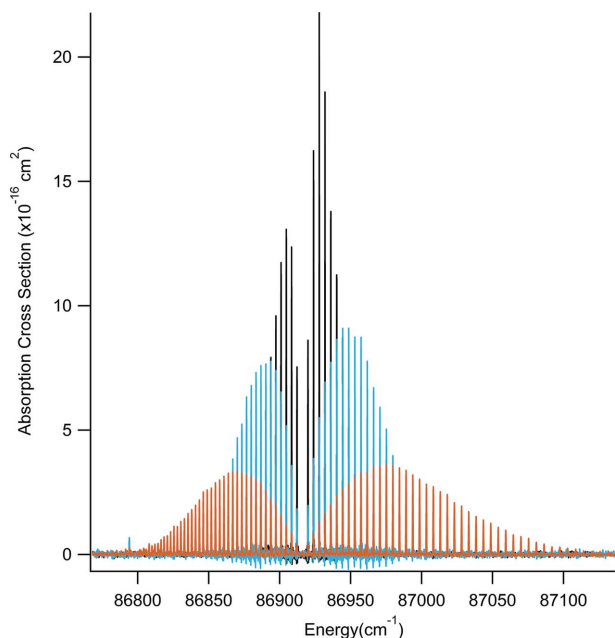
Schematics of the gas sample environment chamber. NV: manual needle valve; VC: vacuum chamber (pressure  $P_i$ ); CG: capacitive gauge (pressure  $P_e$ ); WiC: windowless cell (pressure  $P_e$ ); T1: entrance pipe (conductance  $C_e$ ); Ca1, Ca2, Ca3, Ca4: rectangular section capillaries with conductances of C1, C2, C3, C4, respectively; WiC: switchable windowed cell; LN<sub>2</sub>: liquid-nitrogen jacket. IP are the two  $500 \text{ l s}^{-1}$  ionic pumps of the second stage of differential pumping. TP1 and TP2 are the turbo pumps for the main chamber ( $1500 \text{ l s}^{-1}$ ) and for the free jet setup ( $500 \text{ l s}^{-1}$ ), respectively. If necessary, TP2 can be switched to a  $600 \text{ m}^3 \text{ h}^{-1}$  roots pump without breaking the vacuum. GS: gas supply, for connecting either a gas cylinder or a glass reservoir in order to operate with the vapour pressure of liquid samples. The total length of the vacuum chamber is 1.6 m.

As an example, high-resolution spectra of CO have been recorded for three different temperatures. Fig. 3 shows the high-resolution absorption spectra of the CO  $B^1\Sigma^+$  ( $v' = 0$ )  $-X^1\Sigma^+$  ( $v'' = 0$ ) band at (a) room temperature (windowless cell), (b) high temperature (heated windowless cell) and also (c) very low temperature (supersonic molecular beam). The maxima in the *P* and *R* branch *J*-level distribution shift and each envelope spreads with increasing temperature since the distribution in structure of electronic transitions is essentially given by the thermal distribution of the ro-vibrational levels in the ground electronic state. Following a Boltzmann distribution to describe the rotational population in the ground state, the relative absorbance  $A_J$  of a single rotational line is given by (Herzberg & Spinks, 1950)

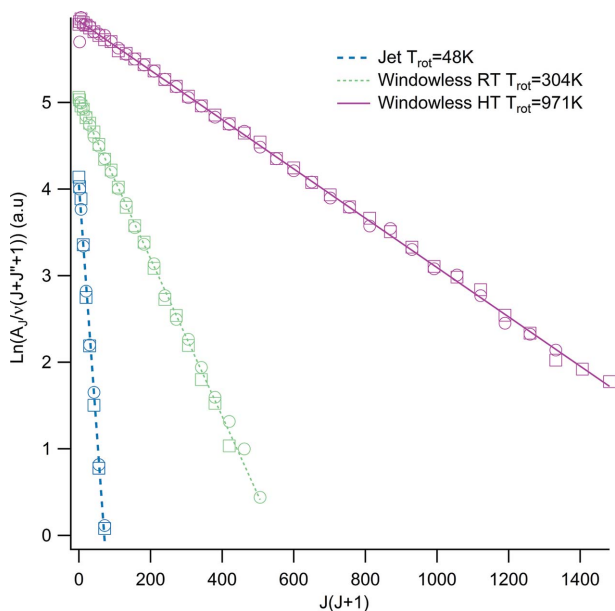
$$\ln\left(\frac{I}{I_0}\right) = A_J \propto \nu(J' + J'' + 1) \exp\left[-\frac{J''(J' + 1)B''hc}{kT_{\text{rot}}}\right], \quad (1)$$

where  $A_J$  is the absorbance of the  $J' \leftarrow J''$  transition,  $J'$  and  $J''$  are the rotational quantum numbers in the upper and ground states, respectively,  $\nu$  is the photon energy of the relevant transition in wavenumber,  $B''$  is the rotational constant of the ground state ( $v'' = 0$ ),  $k$  is the Boltzmann constant, and  $T_{\text{rot}}$  is the rotational temperature to be determined.

In Fig. 4,  $\ln\{A_J/[\nu(J + J'' + 1)]\}$  is plotted *versus*  $J''(J'' + 1)$  for the above-mentioned (a)–(c) cases and  $T_{\text{rot}}$  is deduced


**Figure 3**

Photoabsorption spectrum for the  $B^1\Sigma^+-X^1\Sigma^+(0,0)$  band of  $^{12}\text{C}^{16}\text{O}$ , recorded with (a) the windowless cell at room temperature (blue), (b) the heated windowless cell (orange), and (c) the molecular jet setup (black). A reference room-temperature band oscillator strength was used to determine the column density and calibrate the absolute cross section (Stark *et al.*, 1999a); the instrumental spectral resolution is  $0.23 \text{ cm}^{-1}$ . We assume that only  $v'' = 0$  is populated, except for the high-temperature spectrum for which 1.5% of the molecules are populating the first excited state. For the molecular jet, the backing and background pressures are  $2 \times 10^5 \text{ Pa}$  and  $0.6 \text{ Pa}$ , respectively. The  $P$  and  $R$  branches of the rotational structure are clearly distinguishable; note how the  $J$ -level distribution depends on the temperature (see text for details).


**Figure 4**

Boltzmann plot for the  $B^1\Sigma^+-X^1\Sigma^+(0,0)$  band of  $^{12}\text{C}^{16}\text{O}$  for three different setups: the supersonic molecular jet, the windowless cell at room temperature (RT) and the heated windowless cell (HT). The individual plots are shifted by an arbitrary amount along the ordinate axis for clarity. The slopes of the fitted straight lines are related to the rotational temperature of the gas. The circles correspond to transitions of the  $P$  branch; squares are for the  $R$  branch. No differentiation between the  $P$  and  $R$  transitions has been introduced to the fitting procedure.

from the slope of the fitted straight line; the values found are 304 K, 971 K and 48 K, respectively. This figure illustrates the versatility offered by the various setups that are described in more detail hereafter.

### 3.1. Free supersonic jet expansion

On the FTS branch, a supersonic molecular beam is available in a separated chamber that can be pumped by either a  $500 \text{ l s}^{-1}$  turbomolecular pump (TMP) or a  $600 \text{ m}^3 \text{ h}^{-1}$  root pump (not shown in Fig. 2) depending of the pressure conditions inside this chamber. A slit nozzle ( $1000 \mu\text{m} \times 5 \mu\text{m}$ ) is installed on the jet rod in order to maximize the cold gas column density along the path of the synchrotron beam. The differential pumping can withstand pressures from  $1 \times 10^{-4}$  mbar up to  $1 \times 10^{-1}$  mbar inside the jet chamber during operation. An adiabatic expansion from a high-pressure region into vacuum leads to the cooling of both translational temperature and rotational temperature observed by the reduction of Doppler width of the lines and the modification of the rotational populations of the ground state as described previously. Note that the recorded jet spectrum includes a non-negligible room-temperature contribution due to the partial pressure of background gas along the path of the photon beam. However, this can be corrected by subtracting the room-temperature spectrum; this operation is possible if the room-temperature contribution can be isolated from the recorded spectrum, for instance when the cold spectrum can be clearly identified (Niu *et al.*, 2013). This procedure was followed on the jet molecular spectrum considered in the previous section which presents only a relatively small number of lines contributing to the absorbance (Fig. 3). It is possible to infer the CO column density at room temperature by simply considering the higher  $J$  transitions; therefore, the cooled spectrum is simply deduced by subtracting the room-temperature part corresponding to the background pressure. Ultimately, only lines with  $J$  up to 12 are contributing to the jet spectrum in this example. In all cases, the best results have been observed when the synchrotron beam is as close as possible to the nozzle; otherwise the cold part quickly becomes undetectable as the rod is moved away from the synchrotron radiation beam. Hence, another option is to record an identical spectrum corresponding to a nozzle position far away from the synchrotron beam in order to further remove the background contribution.

### 3.2. Switchable VUV windowed cell

The windowed cell is connected to a gas line and can be inserted into the beam. The cylindrical body of the cell is a stainless steel cylinder connected to a standard gas-handling system located outside the vacuum. Three different lengths (18 mm, 45 mm or 80 mm) can be used, depending on the typical photoabsorption cross section expected for the studied sample. A longer windowed cell (40 cm) can also be installed in place of the windowless one, but this lacks the capability to shift it out of the beam during operation. Outside the main chamber, a pumping system is used to purge the windowed

cell. A capacitive gauge with a range appropriate to the experiment is also part of the gas line. The windowed cell can be used to study gas samples with low photoabsorption cross section in the VUV spectral region down to the transmission limit of MgF<sub>2</sub> windows, which is around 120 nm. This setup is an essential part of the procedure for determining absolute photoabsorption cross sections in the windowless VUV spectral range, as discussed in the next section.

In principle, the true column density can be deduced directly from a precise measurement of the windowed cell length and the absolute pressure. However, in some situations we have observed photolysis processes due to the high photon flux of the incoming white undulator beam ( $\sim 5 \times 10^{15}$  photons s<sup>-1</sup>); this photolysis could bias the measurement. For instance, in the photoabsorption spectrum of CO<sub>2</sub> in the 140–150 nm region, the *A–X* (2,0), *A–X* (3,0) and *A–X* (4,0) band structures of CO are also visible. The partial pressure of CO increases over time and may produce measurement errors, due to the correlated decrease of CO<sub>2</sub> pressure. In order to reduce this phenomenon, it is helpful to have a 100 μm pinhole located on the side of the cell; in such a configuration, the gas is constantly renewed, yielding a reduced partial pressure of the photolysis products. The flowing conditions are stable due to the adjustment of the entrance needle valve. For the CO<sub>2</sub> case, the partial pressure of CO has been estimated to be less than 1% of the base pressure of CO<sub>2</sub>, well below the typical error bars that can be achieved on such a setup (see §5.2). In the case of certain hydrocarbon samples, we noticed a decrease of the transmitted light going through the cell over time. The cracking of hydrocarbon molecules *via* photolysis rapidly leads to carbon contamination on the VUV windows. In such cases, only quick measurements can be made, which are adequate if the structures are broad and do not require high spectral resolution. For instance, a measurement can be achieved in less than 1 min for a spectral line width  $\delta\sigma = 17$  cm<sup>-1</sup>, including the recording of the blank spectra before and after the scan in order to acquire a global average of the background spectrum. In general, the window's transmission can be recovered *in situ* using basically the same O<sub>2</sub>-based technique used to remove the carbon contamination on the FTS reflectors (see §2.3).

### 3.3. Windowless cell

The windowless absorption cell is a stainless steel cylinder with a radius  $r = 10$  mm and a length  $L = 100$  mm, which has been designed to be cooled down to LN<sub>2</sub> temperature. A surrounding annular jacket filled with LN<sub>2</sub> is connected to a dewar in order to keep the level of LN<sub>2</sub> constant during a scan. The flow of LN<sub>2</sub> is controlled using a PID-controlled cryogenic valve; in practice, any temperature between ambient (294 K) and LN<sub>2</sub> (77 K) temperatures can be set. At both ends of the windowless absorption cell, two rectangular capillaries (Ca2, Ca3) are connected to limit the flow of gas into the central chamber pumped by a 1500 l s<sup>-1</sup> TMP (Fig. 2). This first stage of differential pumping is separated from the rest of the beamline by another set of two rectangular capillaries (Ca1,

Ca4) and two 300 l s<sup>-1</sup> ionic pumps which maintain UHV inside the MTF chamber upstream and the FTS chamber downstream. The gas inlet of the system, T1, is composed of several connected tubes of various diameters (from 16 mm to 4 mm), including a 60 cm-long bellow tube inside the vacuum before entering the windowless cell. The extremity of T1 is wrapped around the windowless cell, directly inside the LN<sub>2</sub> bath, in order to increase the amount of cold surface seen by the flowing gas. Outside the chamber a needle valve guarantees a constant flow of gas during a scan, while a set of capacitive gauges covering the  $1 \times 10^{-2}$  Pa to  $1 \times 10^3$  Pa range measure the pressure outside the chamber (Fig. 2). The maximum column density that can be achieved depends on the maximum pressure that can be supported inside the windowless cell by the differential pumping system (see §5.2). Note that the pressure is non-uniform and the column density depends on the pressure distribution inside the capillaries, which makes the extraction of absolute cross-section values from the external pressure measurement challenging (see §4). An extreme-pressure condition was tested in absorption on the very weak *B–X* (2,0) band of <sup>12</sup>C<sup>16</sup>O, where a maximum column density of  $7 \times 10^{17}$  cm<sup>2</sup> was determined from the absorption spectrum using published experimental oscillator strength (Eidelsberg & Rostas, 1990). Note that during the scan the pressure was slightly increasing inside the second stage of differential pumping which is an indication that the ionic pumps had some difficulties tolerating the pressure level; however, an integration time of half an hour was possible and sufficient to achieve a SNR of around 500 in this case. For planetology applications that require the gas to be heated, the same simple design of a T-shape windowless cell has recently been proposed in order to reach high temperatures up to 1000 K (Niu *et al.*, 2015). The hot cell can be easily installed inside the main chamber replacing the LN<sub>2</sub>-cooled cell.

### 4. Absolute photoabsorption cross-section measurements

In practice, the determination of cross sections is deduced from the usual absorption law (Beer–Lambert law):

$$I(\lambda) = I_0 \exp[-N\sigma(\lambda)]. \quad (2)$$

In this expression,  $I$  and  $I_0$  are the transmitted and incident flux, respectively,  $N = nl$  is the column density, with  $n$  the density of absorbing molecules or atoms and  $l$  its length, and  $\sigma(\lambda)$  is the absorption cross-section profile. The procedure to determine the cross section and ultimately the integrated cross section (oscillator strength or *f*-value) from the raw photoabsorption spectrum has been extensively studied in the past (Hudson & Carter, 1968; Chan *et al.*, 1991; Stark *et al.*, 1991; Jolly *et al.*, 1997). Although the reduction of the data may appear trivial, the resulting *f*-values can be affected by low instrumental resolution, and a direct reduction of equation (2) could yield large errors when absolute measurements are needed, especially when lines are sharp compared with the instrumental line width. This is the main reason why direct use of the Beer–Lambert law to determine oscillator strength has

since been rarely used in the far VUV (especially in the windowless region); the usual broadband techniques, for instance grating-based spectrometers, present an insufficient resolution to give precise measurements, particularly on atomic species and small molecules.

To overcome this difficulty, various techniques have been employed: for instance, mixing the sample with a high-pressure transparent gas in order to increase the line width by pressure broadening (Jolly *et al.*, 1997). The curve of growth is another technique which allows the determination of line oscillator strength or column densities without the required spectral resolution by plotting the equivalent width of a line over a range of optical thickness (Aller, 1991). Measurement at various pressures and extrapolation to zero column density is also an option to obtain the true integrated cross section (Stark *et al.*, 1993; Yoshino *et al.*, 1995). In the past years, models based on the coupled-channel Schrödinger equation have emerged giving access to an accurate description of experimental results especially when dense interacting electronic states are encountered as it is the case of diatomic molecules in the VUV spectral region (Lewis *et al.*, 1999, and references therein). These sophisticated models can take advantage of high-spectral-resolution VUV photoabsorption measurements given by FT or laser-based spectroscopy in order to improve the electronic structure description through perturbations identification and pre-dissociation line widths determination, and also band oscillator strengths measurement. For instance, users of the VUV FTS have developed numerical simulations based on model spectra convolved with the FTS apparatus function in order to reproduce experimental data. Eventually, the fitting procedure gives line positions, line width and  $f$ -values with an uncertainty depending on the spectral resolution and the SNR (Heays *et al.*, 2011); deperturbation analysis can also be performed (Heays *et al.*, 2014).

However, for absolute cross-section measurements, an accurate column density value is required for these techniques. As mentioned in the previous section, the column density of a continuously flowing absorption cell is difficult to evaluate. In general, the procedure is made possible by referencing the broad spectral range covered by the FTS to a few lines or a single isolated ro-vibrational band measured in the VUV windowed range and known from the literature. For instance, the  $^{12}\text{C}^{16}\text{O}$   $B-X$  (0,0) band reference was recently used to determine the CO column density in the pre-dissociation region of various CO isotopologues (Heays *et al.*, 2011; Eidelsberg *et al.*, 2012). This reference was recorded using a VUV laser-based spectrometer with a LiF windowed cell, and the full band integrated absorption cross section was determined from measuring a few individual rotational lines (Stark *et al.*, 1999a). This technique works particularly well when the cross sections of the reference band and the recorded spectrum are not too different; otherwise, the band reference absorption could be either too weak or too strong for a precise column density determination. Furthermore, we have seen that very often it is preferable to use the windowless cell even in the low energy range as the undulator high flux can induce

photochemical reactions, leading to difficulties in reduction of the data (§3.2).

In the following sections, we present the FTS procedure, which allows derivation of absolute photoabsorption spectra in the VUV windowless spectral region when a single spectral window is recorded in the VUV windowed spectral region and when the cross section is not well adapted to the determination of the windowless part of the spectrum. Future developments allowing the possibility of inferring column densities inside a flowing cell, therefore avoiding the use of any absolute reference, are also discussed.

#### 4.1. Absolute photoabsorption measurements by means of internal calibration

In the windowless VUV range, a major difficulty is the measurement of the true column density during a scan. The density of absorbing species inside the windowless cell can be directly deduced from the pressure measurement outside the chamber. However, we will see that the relation is not linear as the gas flow is not necessarily in a molecular regime.

Both windowed and windowless absorption cells are used in order to measure the absolute column density value throughout the full VUV spectral range. The first step involves the measurement of a single undulator spectral window with the windowed cell setup. Note that the procedure has been tested on a spectrum presenting broad structures in order to remove any possible instrumental saturation effects due to insufficient resolution. The cross section is deduced by calculating the column density knowing the cell length and the pressure inside the cell. Then, the windowed cell is removed from the beam and exactly the same spectral window is recorded with the windowless cell. One complication lies in the fact that the pressure/column density relation is not linear. In the typical pressure range covered, the gas flow goes from a molecular regime to an intermediate regime leading to more complex flow dynamics. Hence, the procedure has to be carried out over several photoabsorption spectra at various entrance pressures ( $P_e$ ). Column densities are determined by using the absolute cross section previously measured with the windowed cell. Finally, the calibration curve is applied throughout the full VUV spectral range including the windowless part of the spectrum.

The rectangular cross sections of the capillaries Ca1, Ca2, Ca3 and Ca4 have been chosen in order to fit the shape of the converging astigmatic undulator beam entering the FTS after being reflected by the MTF toroidal mirror; their dimensions are 7.5 mm  $\times$  4.5 mm, 7 mm  $\times$  4 mm, 7 mm  $\times$  4 mm and 6 mm  $\times$  2 mm, respectively. Their lengths (15 cm) have been chosen considering space and vacuum constraints inside the main chamber. In order to fully model the windowless cell setup, it is necessary to introduce a complete description of the gas flow as the three regimes (molecular, intermediate and laminar) can be encountered over the range of entrance pressures used, from 0.1 Pa to a few 100 Pa. However, the entrance line (T1) includes various sections of different diameters with a particular geometry and a 60 cm-long bellow

tube, and makes difficult a vacuum conductance calculation using a simple standard model. Nevertheless, in order to describe the cell geometry analytically in all steady-state flow regimes, we model the rectangular cross-section capillaries Ca2, Ca3 and the inlet pipe T1 as simple long circular cross section tubes (length  $\gg$  diameter) of conductance  $C_2$ ,  $C_3$  and  $C_e$ . We consider equivalent tubes of diameter and length ( $D_e$ ,  $L_e$ ) for  $C_e$ , and ( $D_c$ ,  $L_c$ ) for the identical Ca2 and Ca3 capillaries.  $C_c$  will be defined as the windowless cell capillaries' total conductance  $C_2 + C_3$  and will be calculated analytically. The only missing parameters,  $D_e$  and  $L_e$ , will be determined through a least-squares-fitting procedure, comparing the experimentally measured column density from a reference absorption spectrum with that determined from our model.

The general expression of the total conductance  $C_T$  for a circular-section tube in an intermediate flow regime is given by the semi-empirical Knudsen's formula (Roth, 2012):

$$C_T = C_v + C_m \frac{1 + \varepsilon \bar{P}}{1 + 1.24 \varepsilon \bar{P}}, \quad (3)$$

where  $C_v = k_v \bar{P} = (\pi/128\eta)(D^4/L)\bar{P}$  and  $C_m = (1/6)(2\pi RT/M)^{1/2}(D^3/L)$  are the conductance ( $\text{m}^3 \text{s}^{-1}$ ) in the laminar and molecular regimes, respectively;  $\varepsilon = D(M/RT)^{1/2}/\eta$ .  $M$ ,  $T$  (K),  $R$ ,  $\eta$  ( $\text{Pa s}^{-1}$ ),  $D$  (m) and  $L$  (m) are the molecular weight, temperature, gas constant, gas viscosity, diameter and length, respectively, of the tube.  $\bar{P}$  (Pa) is the average pressure in the section connecting two volumes of different pressures, and  $S$  ( $\text{m}^3 \text{s}^{-1}$ ) is the TMP effective vacuum speed in the chamber. Assuming a molecular regime in the main vacuum chamber VC,  $S$  has been determined considering the theoretical TMP vacuum speed and the pipe length connecting the pump to VC. We consider that the outgassing is negligible compared with the typical range of pressure inside VC. In this case, the gas flow rate,  $Q$  ( $\text{Pa m}^3 \text{s}^{-1}$ ), is conserved through the system and can be expressed as

$$Q = (P_e - P_c)C_e = (P_c - SP_f)C_c = SP_f, \quad (4)$$

where  $P_e$  and  $P_f$  are the entrance and the main vacuum chamber pressures (Fig. 2). We first determine the pressure  $P_c$  inside the windowless cell in the intermediate flow regime, and then calculate the column density and compare the values with experimental data in order to validate the model. The pressure distribution in the capillaries must be computed in order to fully derive a correct value for the column density.

We assume that  $P_e \gg P_f$ , then (4) leads to

$$(P_e - P_c)C_e = P_c C_c. \quad (5)$$

The general expression for the conductance (3) yields

$$(P_e - P_c) \left\{ C_{e_v} + C_{e_m} \frac{1 + \varepsilon_e [(P_e + P_c)/2]}{1 + 1.24 \varepsilon_e [(P_e + P_c)/2]} \right\} = P_c \left\{ C_{c_v} + C_{c_m} \frac{1 + \varepsilon_c [(P_e + P_c)/2]}{1 + 1.24 \varepsilon_c [(P_e + P_c)/2]} \right\}. \quad (6)$$

The development leads to a fourth-order polynomial equation of the unknown  $P_c$  pressure on the windowless cell involving its geometrical parameters and the entrance pressure  $P_e$ . Note that the T1 conductance,  $C_e$ , can only be estimated, and the unknown ( $D_e$ ,  $L_e$ ) values are the only missing parameters to fully describe the absorption cell. These parameters are determined through a least-squares fitting procedure. Indeed, a calculated column density curve can be compared with data reduced from experimental measurements from  $P_c$  and  $L$ . However, it has been observed that the gas flowing through the capillaries leads to a pressure gradient across the capillaries that cannot be neglected if a complete description of the setup is to be made (Mercier *et al.*, 2000). Thus, the total computed column density (Col) is

$$\text{Col} = P_c L + 2 \int_0^{L_c} P(x) dx. \quad (7)$$

We use equation (5) from Mercier *et al.* (2000) to determine  $P(x)$ :

$$P(x) = K_0 + [(K_0 - P_c)^2 - xK_2]^{1/2}, \quad (8)$$

where  $K_0 = C_2 C_m / 1.24 k_2 v$ ,  $K_2 = 2Q / k_2 v L_c$  and  $Q = 2P_c^2 k_2 v [1 - (C_2^2 / S^2)] + (P_c C_2 C_m / 1.24) [1 - (C_2 / S)]$ . The calibration curve relating the entrance pressure  $P_e$  and the column density Col is determined experimentally and compared with the model in order to deduce the missing parameters ( $D_e$  and  $L_e$ ) by a least-squares fitting procedure as described below.

#### 4.2. Calibration of the model by use of the O<sub>2</sub> case

The VUV photoabsorption spectrum of <sup>16</sup>O<sub>2</sub> has been the subject of several investigations not only because it is an important component of the photochemistry of the atmosphere but also because it is a simple homonuclear diatomic molecule showcase. The vibrational progression converging to the ionization potential, 12.07 eV, is quite complicated with large interaction between Rydberg and valence states and has not yet been fully described (Lewis *et al.*, 2002). Three diffuse bands belonging to the  $E^3 \Sigma_u^-$  progression are particularly interesting as a test for the model developed in the previous section. These three diffuse bands are known in the literature as the longest, the second and the third band and are located at 80390  $\text{cm}^{-1}$ , 82900  $\text{cm}^{-1}$  and 85200  $\text{cm}^{-1}$ , respectively, and thus are within the near VUV spectral region where windows can be used. First, we have measured the absolute photoabsorption cross section at room temperature for these bands using the MgF<sub>2</sub> absorption windowed cell at a moderate spectral resolution of 3.5  $\text{cm}^{-1}$ . A direct comparison of the FTS experimental data with two previous measurements (Lewis *et al.*, 1988; Lu *et al.*, 2010) is presented in Fig. 5 for the longest band recorded with a line width of approximately 3  $\text{cm}^{-1}$  and 10  $\text{cm}^{-1}$ , respectively. The three curves overlap satisfactorily within the claimed experimental uncertainties: 10% for Lu *et al.* and 4% for Lewis *et al.* The longest, the second and the third band of <sup>16</sup>O<sub>2</sub> offer an interesting case study as their typical cross sections are in the range

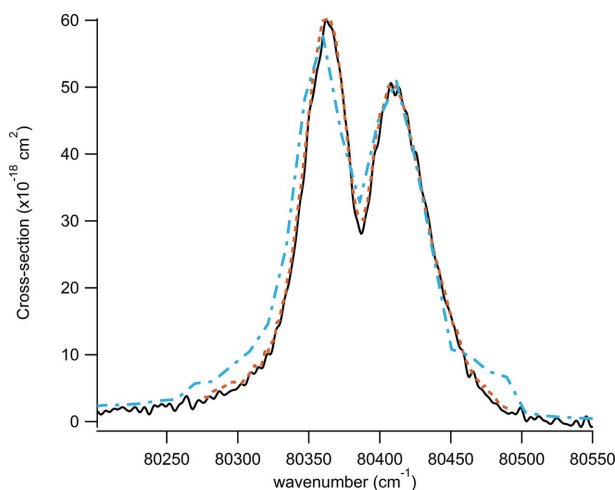


**Figure 5**

Experimental photoabsorption cross section for the mixed-valence Rydberg state [ $E^3 \Sigma_u^- v = -X^3 \Sigma_g^- v(0, 0)$ ] also known as the longest band of  $^{16}\text{O}_2$ . In black (solid), FTS data recorded using the  $\text{MgF}_2$  windowed cell. In orange (dash), blue (dash-dotted): two references from the literature [Lewis *et al.* (1988) and Lu *et al.* (2010), respectively] have been included for comparison. The data are digitized from the first reference Fig. 1 and obtained from the MPI-Mainz spectral atlas for the latter one (Keller-Rudek *et al.*, 2013). The FTS cross section is within the claimed precision of the references, *i.e.* 5% and 10%, respectively.

2–50 Mbarn. Therefore, it has been possible to cover a range of entrance pressures  $P_e$  (0–180 Pa) going from the molecular up to the intermediate flow regime and still be able to reduce column density data from unsaturated bands. The next step involves the windowless absorption cell, with which the same bands are recorded for a set of entrance pressures  $P_e$ , and the absolute photoabsorption cross sections are used to infer the corresponding column densities. The resulting least-squares-fitting curve is close to the experimental data points, as can be inferred from Fig. 6 which shows the effectiveness of the flow modelling. The fitting procedure yields the missing parameters:  $De = 0.005$  m and  $Le = 1.9$  m. Note that the overall physical length of the T1 entrance tubing system is  $L1 = 0.8$  m and the typical diameter is 0.006 m. The difference could be explained by considering that T1 is principally made of a 0.6 m-long bellow tube that probably reduces the conductance compared with a smooth pipe. Nevertheless, the aim of this study is to provide a set of experimental parameters in order to evaluate the calibration curve, especially if the full range of required entrance pressures  $P_e$  cannot be measured due, for instance, to the saturation of the band taken as a reference for a particular sample. As an illustration, the fitting procedure has been carried out over experimental data points recorded only between 0 and 50 Pa, and we see that the extrapolated curve up to 180 Pa fits the experimental points within a typical  $\pm 5\%$  error (Fig. 6).

Further improvement would require numerical simulation like direct simulation Monte Carlo methods based on more sophisticated models to describe the flow dynamics of the setup accurately. This approach might give a better total column density measurement, and thus improve the absolute photoabsorption spectra determination in the windowless

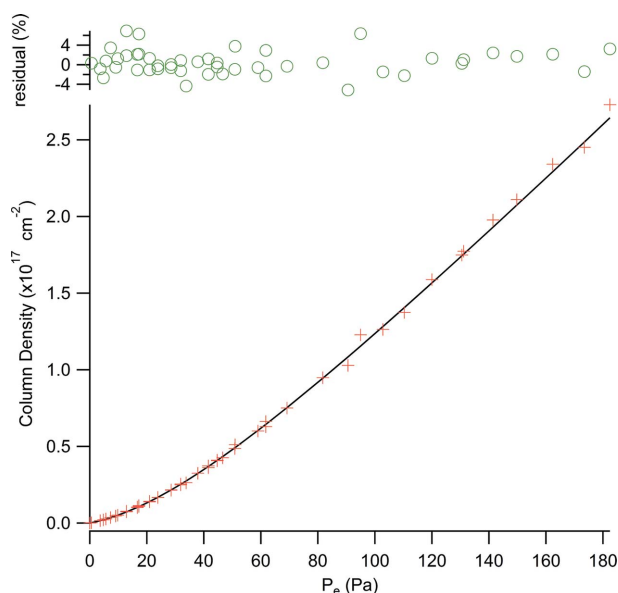


**Figure 6**

Plot of the total column density inside the windowless absorption cell related to the entrance pressure ( $P_e$ ). The experimental points have been determined from recorded spectra of the longest, the second and the third bands of  $^{16}\text{O}_2$  belonging to the  $E^3 \Sigma_u^-$  progression. The modelling (solid line) is based upon the flowing equation related to the geometry of the cell and to the pumping conditions. The standard deviation of the residual error is 2.5% (see text for details).

setup. Moreover, it should be possible to fully model the flowing conditions of any gas sample and then produce a calibration curve even without any absolute reference. Nevertheless, our methodology leads to the determination of a calibration curve that can be used for a particular sample and geometry, over the full VUV spectral range. A typical experimental procedure involves the determination of the column density calibration curve for one particular spectral window in the VUV windowed region. Then, the complete VUV spectrum can be recorded using the windowless setup which provides better SNR plus a significant reduction of possible degradation of the sample that can be faced in the windowed cell, especially for high spectral resolution scans requiring longer integration time. Additional sources of uncertainties specific to the VUV FTS will be detailed in the next section.

## 5. VUV FTS intrinsic error sources and photoabsorption measurement outcomes

In addition to the column density estimation, the precision and accuracy in photoabsorption measurement is primarily governed by the precision in determination of the line parameters (line height, integral, line width) and of the level of the background continuum. Concerning the line parameters, under-resolved spectral line measurement is a common problem in high-resolution absorption spectroscopy known as instrumental bandwidth effect. We already mentioned that such an effect can induce large errors after reduction of the data (Chan *et al.*, 1991), but can also be overcome if the

features are not too blended, or if the spectrum is moderately under-resolved (Brown *et al.*, 1983).

When considering the background continuum, the specific spectral error is related to the particular nature of the VUV FTS, as it is a wavefront-division scanning interferometer. In general, spectral errors in FT spectrometry may be induced by sampling position errors. As far as the fast Fourier transform (FFT) algorithm is concerned, the regularity of the sampling comb (in terms of path differences) is fundamental, and such errors result in various spectral deformations. Some are well known and are addressed by classical procedures during data processing. These are principally: optical path difference (OPD) origin errors (when asymmetrical cosine FFT is used), source spectral inhomogeneity (chirping), and scan trajectory slow drifts, which can be addressed by Forman techniques or similar ones (Forman *et al.*, 1966), in the spectral domain, or by local interpolation techniques in the OPD domain (Kaupinen *et al.*, 1978). However, in the case of the VUV FTS, sampling errors may produce an apparent random shift (jitter) of the undulator spectral shape. The phenomenon is illustrated in Fig. 7(a), which shows experimental spectra computed from several successive single scans, in the same undulator spectral window. It should be emphasized that this shift of the spectrum is only apparent: it is not a perturbation of the true spectral scale, as illustrated in the figure by the fact that the few sharp lines shown are not shifted at all. We now focus on the interpretation of and the possibility to partially correct this kind of error. This is an important issue since the jitter results in a perturbation of the background level, and thus a part of the error in the measured absorption spectrum. The FTS photoabsorption error budget is also presented in §5.2.

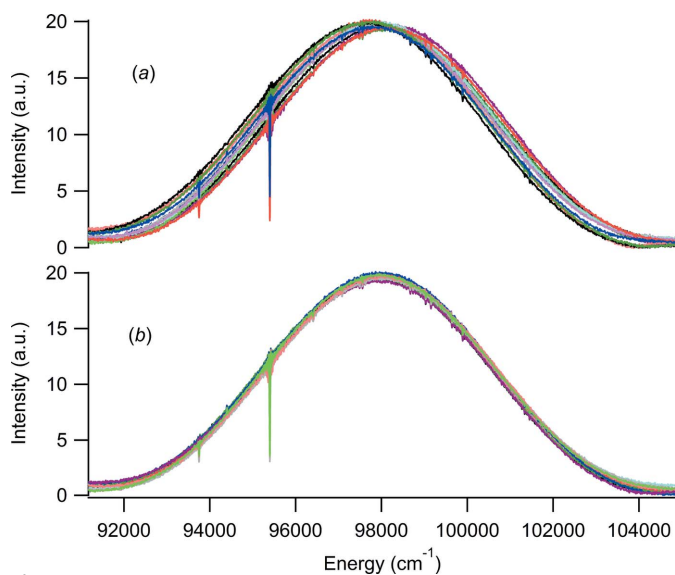


**Figure 7**  
 (a) Set of ten independent undulator pink-beam measurements recorded successively; the jitter amplitude on the side of the undulator shape reaches 8.4%. (b) Same set of data after application of the phase correction procedure; the dispersion is now 2.4%, *i.e.* a reduction by a factor of 3.5. Note that the position and shape of the atomic sharp lines coming from the beamline gas filter are not affected.

### 5.1. Interferogram processing

A major difference between wavefront-division (WD) and amplitude-division interferometers is that, in the WD case, in principle, the interference field cannot be uniform in terms of OPD; it contains roughly one fringe in the case of the VUV FTS (de Oliveira *et al.*, 2009). Consequently, the detected state of interference varies along two axes: the time/OPD axis (scanning) and also the spatial axis transverse to the fringe system. In other words, the detected interferometric signal may vary either by scanning (the normal way) or by a shift of the spatial fringe system in the detector plane, thus producing a spurious apparent change of OPD, and therefore a sampled interferometric signal affected by sampling position errors.

Two kinds of causes may produce such errors. First, slow drifts of the interferometer geometry during a scan can change the sampling interval and therefore produce mainly line distortion and spectral scale error. These are not specific to WD FT spectroscopy, and are addressed as mentioned in the previous section. Second, such fringe shifts may occur from vibratory phenomenon due to instabilities of the source beam, but also (and mainly) from spurious rotations of the interferometer mirrors, in particular when scanning is in progress. As far as mechanical vibrations are involved, *e.g.* from the scanning system, or from mirrors on the beamline, the sampling error function relative to one particular scan belongs to a bandpass random process, producing a different outcome from scan to scan. To understand their influence on the measured spectrum, it is necessary to compare the OPD/spectral error characteristics with either the interferogram or the spectrum structure. Both approaches are indeed equivalent, but the OPD approach is easier to understand, and will be used hereafter. In this discussion, it can be assumed that the scanning speed is constant on average, making the theoretical OPD variation proportional to time. Therefore, we can use indifferently the OPD or the time scale, as far as the interferogram or the perturbing vibrations are concerned.

In the specific case of absorption spectroscopy from an undulator source, the background spectrum and the absorption lines behave differently in the OPD domain. The background shape description, which is an unstructured and broad Gaussian with a 7% full width at half-maximum (FWHM) of the central photon energy, is related to interferogram samples close to the zero path difference, at most a few tens of wavelengths on both sides of zero OPD. This is one- to two-hundreds of samples, depending on the average wavelength. On the other hand, even for moderately broad lines, interferometric information is spread over several thousand wavelengths, at least. Let us use a typical spectrometer configuration (de Oliveira *et al.*, 2009) and switch from OPD to time domain. With a free spectral domain down to  $\lambda = 40$  nm, samples are separated by  $\sim 20$  nm (OPD), or  $\sim 10$  nm (displacement). With a scanning speed of  $150 \mu\text{m s}^{-1}$ , this is roughly 0.07 ms per sample. In other words, the information about the broad background is concentrated into less than  $\sim 14$  ms (on each side of the OPD origin), whereas sharp lines are spread over at least seconds, generally much more. These

durations have to be compared with the correlation time of the noise function. As mechanical vibrations are involved, and taking into account the mechanical structure of the interferometer, we consider that the vibration spectrum is essentially limited to the 10–100 Hz band, as a rough estimation, which will be confirmed later. In other words, the correlation time of the noise function is comparable with (or larger than) the duration of the undulator interferometric signal (starting at  $OPD = 0$ ), and is much smaller than the duration of the interferometric signal from any reasonably narrow spectral line.

This explains why the perturbation of the spectral components, namely narrow lines and undulator broad spectrum, are very different. In the case of narrow lines, the ergodic principle applies to each single scan, and the spectrum undergoes statistical perturbation depending on the r.m.s. sampling error: this is classically studied to assess the required sampling accuracy for accurate spectra (Chamberlain, 1979). If the r.m.s. error is kept within  $\lambda/15$  in OPD, there is a negligible perturbation of the line shape, and a limited loss of its amplitude. In contrast, the interferometric signal from the undulator spectrum can be perturbed by few correlation times, even by less than one. The perturbation is therefore not statistical for one single scan: the result is in an apparent shift and/or a distortion of the spectral shape which changes randomly from scan to scan as illustrated in Fig. 8. Obviously, the main consequence of this jitter of the background spectrum in absorption experiments is a significant error in the determination of absorption cross section. The jitter amplitude (*i.e.* fluctuation of the background level at half-maximum of the spectral background) is generally between 15% r.m.s. (the worst cases) and 4% r.m.s., producing significant cross-section errors. However, in most cases the jitter noise can be reduced with a post-acquisition correction process performed on the interferograms. Besides, averaging on several scans to obtain a better estimation of the spectral shape also improves the dispersion error r.m.s. by the square root of the number of averaged scans.

A more refined processing aims to reduce the error for each scan, and then average. To this end, it is necessary to have at least partial knowledge of the sampling position noise. Fortunately, the design of the VUV FTS includes a secondary interferometer, which uses part of the He–Ne monomode stabilized control laser beam to feed the VUV interferometer, producing a separate ‘red interferogram’. As the same VUV reflectors are used, this interferogram undergoes the same perturbations as the VUV interferogram. However, as the red beam path includes several additional steering mirrors, any perturbation from these mirrors (vibrations) is injected into the red interferogram, but not in the VUV interferogram. Similarly, any perturbation intrinsic to the VUV beam is not present in the red interferogram. Nevertheless, a strong correlation should exist between VUV and ‘red’ perturbation, which should allow at least a partial correction of the VUV interferogram, based on the ‘red interferogram’ perturbation. To this end, we use a standard tool of Fourier analysis to recover long-range sampling errors (Kauppinen *et al.*, 1978;

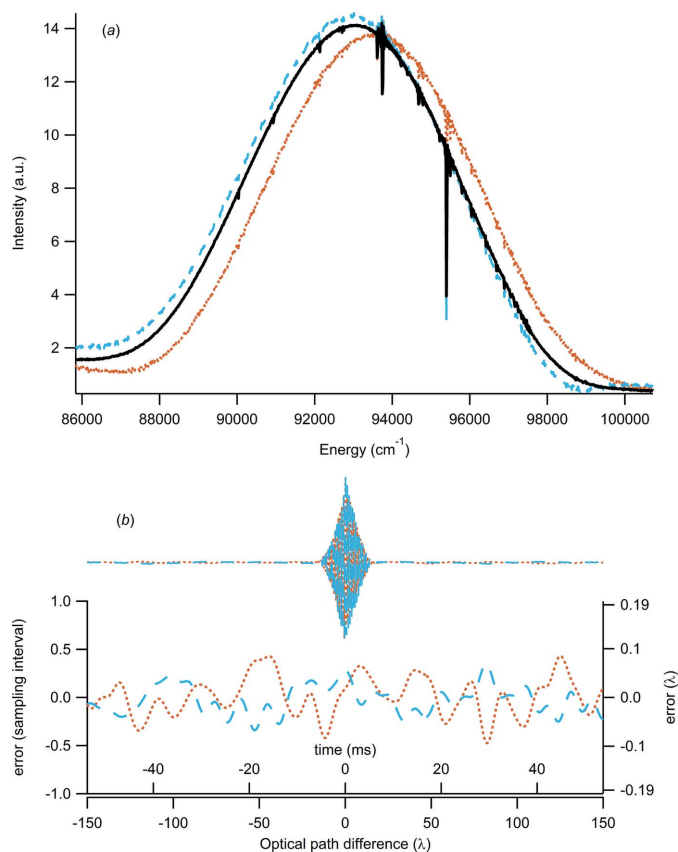


**Figure 8**

(a) Two undulator spectra out of a series of 12 successive interferograms, and (b) their associated interferograms and error functions; the error is computed from the auxiliary ‘red interferograms’. The black solid line spectrum is an average of the 12 corrected spectra, which can be considered as a good approximation of a jitter-free spectrum. Note the roughly linear error across the central fringe packet for the orange dotted trace, associated with the large shift of the spectrum. In contrast, the blue dashed trace is associated with a smaller shift in the inverse direction, and also some distortion of the spectral shape. The r.m.s. of the error function is roughly 0.2 sample interval, corresponding to  $\lambda/25$  for  $\sigma = 93000 \text{ cm}^{-1}$  (107.5 nm).

de Oliveira *et al.*, 2009). This tool is a phase demodulation of the ‘red interferogram’, yielding the position error function relative to the sampling comb. In a first step, we checked the validity of our model by computing a synthetic interferogram, assuming a Gaussian spectral source similar to the undulator shape, and introducing sampling errors computed from the red interferogram of a real scan; the result obtained is very similar to a typical experimental set of recorded spectra. Next, an approximated correction algorithm based on a local interpolation of the interferogram, according to the sampling error function, was applied to this set of interferograms. We observed a reduction of the jitter noise amplitude by a factor greater than 10, limited by the correction algorithm. Finally, the process was implemented for a real set of recorded scans, by adjusting the error function (as extracted from the red interferogram) for the best reduction of the jitter in the VUV spectrum. This simple adjustment, which consists of the application of a multiplicative coefficient on the computed error function, yields usually an improvement of the jitter by a

factor of 2 to 3 (Fig. 7*b*). More complex adjustments are under test, based on the frequency analysis of the position error function, for frequency-dependent adjustment of the error function before correction of the VUV interferogram.

### 5.2. Photoabsorption cross-section error analysis

In this section, an error analysis leading to typical uncertainties of the absolute photoabsorption cross section is established based on experimental data. Typically, three sources contribute to the uncertainty in the absolute photoabsorption cross-section measurements: the uncertainty in the column density determination, uncertainties associated with the measurement SNR, and a third component associated with unresolved spectral structures. This last source of error has been discussed extensively in the literature and already mentioned, and will be neglected hereafter. An expression for the fractional error can be derived from (2) assuming  $\Delta I = \Delta I_0$  (Stark *et al.*, 1999*b*),

$$\left(\frac{\Delta\sigma}{\sigma}\right)_{\text{noise}} = \frac{\Delta I_{\text{noise}}}{I_0 N \sigma} \left[1 + \exp(2N\sigma)\right]^{1/2}. \quad (9)$$

The uncertainty is linked to optical depth ( $N\sigma$ ) for a given SNR. When it is possible, the absorption must be kept between 40% and 70%, as (9) presents a broad minimum within this interval. For the purpose of the following noise study, we will assume a 50% absorbance. In our case, a fourth source of error must be considered:  $\Delta I$  is not only related to the noise in the spectrum,  $\Delta I_{\text{noise}}$ , but also must include a contribution due to the jitter effect,  $\Delta I_{\text{jitter}}$ , mentioned in the previous section. Note that  $\Delta I_{\text{noise}}$  and  $\Delta I_{\text{jitter}}$  are not correlated but are both dependent on the energy range. Similarly,

$$\left(\frac{\Delta\sigma}{\sigma}\right)_{\text{jitter}} = \frac{\Delta I_{\text{jitter}}}{I_0 N \sigma} \left[1 + \exp(2N\sigma)\right]^{1/2}. \quad (10)$$

If the sources of error are statistically independent, then the overall cross-section uncertainty can be expressed by

$$\left(\frac{\Delta\sigma}{\sigma}\right)^2 = \left(\frac{\Delta N}{N}\right)^2 + \left(\frac{\Delta\sigma}{\sigma}\right)_{\text{noise}}^2 + \left(\frac{\Delta\sigma}{\sigma}\right)_{\text{jitter}}^2, \quad (11)$$

where  $\Delta N/N$  is the uncertainty of the absorbing column density. A plot of  $(\Delta\sigma/\sigma)_{\text{noise}}$  and  $(\Delta\sigma/\sigma)_{\text{jitter}}$  is presented in Fig. 9, covering most of the instrument spectral range from 45000 to 125000  $\text{cm}^{-1}$ . The plot is the result of numerous experimental recordings over two years of operation and can be seen as typical values of the FTS branch. Note that these values have their own uncertainty due to the diversity of experimental conditions seen over time during the data collection. For instance, the FTS settings and the external conditions regarding vibrational noise inside the facility (transmitted from the floor) may have direct consequences on the jitter effect.

Of course the SNR depends strongly on the spectral resolution and the integration time. The SNR in the FTS increases as the square root of the line width and the square root of the integration time (Davis *et al.*, 2001);  $(\Delta\sigma/\sigma)_{\text{noise}}$  is a normalized value to an instrumental line width of  $\delta\sigma = 0.45 \text{ cm}^{-1}$ , and

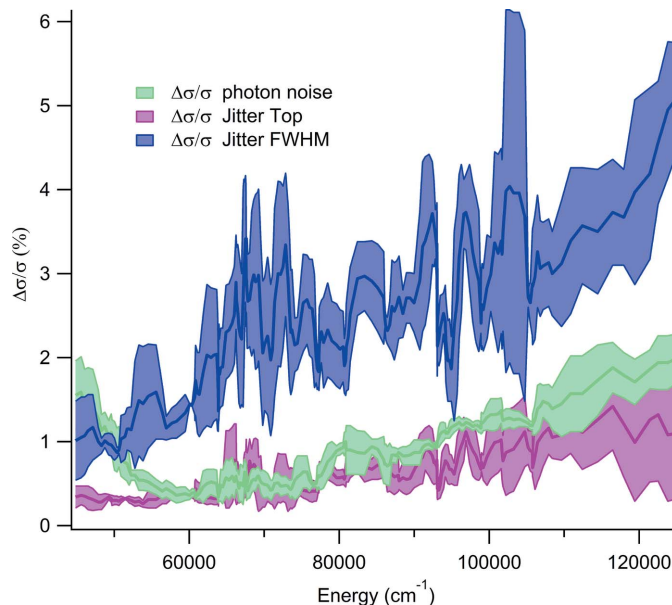


**Figure 9** Uncertainty of the absolute cross-section measurement for different sources of error (%) related to the spectrometer. The photon-noise-induced fractional error of the undulator envelope is shown in green, the jitter error on top in purple, and at FWHM in blue. The  $1\sigma$  dispersion of the collected data is superimposed on the trace. The principal source of error originates from the jitter effect and increases as we move away from the top of the undulator envelope. In order to minimize this effect, and when a large spectral range has to be covered, the stitching of the spectral windows is performed typically at half-maximum of the undulator envelope.

an effective integration time of 15 min, with the current in the storage ring being 430 mA. These values provide a typical photon noise limited SNR of 400, with variations related to the energy spectral range investigated.  $(\Delta\sigma/\sigma)_{\text{jitter}}$  is indirectly integration-time-dependent, through the number  $N_s$  of averaged scans in the spectrum,  $\Delta I_{\text{jitter}} \propto (1/\sqrt{N_s})$ .  $(\Delta\sigma/\sigma)_{\text{jitter}}$  at the top and on the side at half width of half-maximum of the undulator envelope are presented and normalized to  $N_s = 20$ , which is the typical number of scans for a single spectral window.

The contribution to the uncertainty of  $\sigma$  from the noise in the spectrum is in general below 1% and increases slightly in the low and high energy range because of the SNR degradation. Note that below 60000  $\text{cm}^{-1}$  the SNR is decreasing partly because of a decrease in reflectivity of the FTS interferometer's SiC coating. Note also that, in order to extend the energy range of the FTS, slightly elliptical polarization must be used (see §2.2) to reach lower photon energies; the added horizontal linear contribution is less efficient in terms of photon flux because the plane of incidence of the optics is horizontal in that section of the beamline, especially considering that the beam undergoes a double reflection with a  $45^\circ$  incidence angle onto the FTS reflectors. We also observe that the jitter amplitude is minimal at the top of the envelope and increases as we move towards the sides of the pseudo-Gaussian shape of the undulator envelope, as mentioned in the previous section. In practice, the stitching together of the spectral windows is typically performed at their half-

maximum, therefore  $(\Delta\sigma/\sigma)_{\text{jitter}}$  at half-maximum values can be considered to be the typical upper limits. It can be seen from Fig. 9 that the jitter amplitude increases with energy. This trend is at least partially related to the size of the detected VUV interference fringe: as the fringe spacing is proportional to the wavelength, as we go further into the VUV the detected signal becomes more and more sensitive to the vibrational noise conditions and the jitter increases.

In practice, it is quite difficult to give definitive and general error values for the VUV FTS apparatus. Nevertheless, from the considerations developed above, we can set an upper limit considering all possible sources of error. The uncertainty on the column density  $(\Delta N/N)$  originates from the accuracy of the capacitive gauge pressure measurement and the cell length estimation, with a standard deviation of 0.2% of reading and 0.5%, respectively. The synchrotron experimental hall temperature is regulated to  $20^\circ\text{C} \pm 1^\circ\text{C}$ ; the influence on the capacitive gauge measurement can be considered negligible. The jitter contributes significantly, as can be inferred from Fig. 9; at half-maximum,  $(\Delta\sigma/\sigma)_{\text{jitter}} \simeq 3\%$  and can be considered a typical upper value. The contribution from the noise,  $(\Delta\sigma/\sigma)_{\text{noise}}$ , is below 1%. If we assume uncorrelated uncertainties, this leads to a global typical uncertainty of  $(\Delta\sigma/\sigma) \simeq 3.2\%$  for the absolute photoabsorption cross-section measurements. A recent FTS experimental study gave similar values for the integrated cross sections of the  $B-X$ ,  $C-X$  and  $E-X$  systems on CO isotopologues (Stark *et al.*, 2014). Moreover, the error estimated from the modelling performed on  $\text{O}_2$  in the previous section gives a standard deviation of 2.5%; most of this error is expected to come from the jitter. The jitter is a major error source; important efforts both preventive (reducing possible sources of vibration on the beamline) and also in the post-treatment of the data (see §5.1) have been made and are still underway to improve this aspect. It may happen that some experimental conditions give a larger error, mainly because of difficulties in column density determination in the flow cell and/or the amplitude of the jitter; the figures given above can be considered as the most probable estimate of the accuracy of the measurement.

As mentioned previously, the fractional error depends on the optical depth in such a way that the error can be considered minimal for absorptions between 40% and 70%, which is why we assumed a 50% absorbed spectrum so as to set our photoabsorption cross-section error budget estimation. The experimental setup allows in general the adjustment of the gas pressure inside the cell in order to fulfil this condition. However, the column density is limited in the windowless cell due to the differential pumping, which directly limits the minimal detectable cross section, which is related to the maximum column density and the SNR. The maximum column density that can be achieved in the windowless cell is  $\sim 5 \times 10^{17} \text{ cm}^{-2}$ ; for a typical noise level,  $\Delta I_{\text{noise}}/I = 0.25\%$  at the top of the undulator envelope and, if the fractional error on the measured cross section is kept below 5%, then  $\sigma_{\text{min}} \simeq 1.5 \times 10^{-19} \text{ cm}^2$ . This value can be considered a lower limit of detection in the ideal case where the column density can be freely adjusted. However, liquid samples with limited vapour

pressure or study of expensive isotopologues can also impose restrictions on the flowing conditions inside the cell. The same parameters are used for the estimations of the other setups in the gas sample environment chamber and are presented in Table 2.

## 6. Conclusions and future developments

We described a state-of-the-art experimental end-station for ultra-high-resolution absorption spectroscopy in the VUV which combines a windowless absorption cell, a windowed absorption cell and a jet setup. The branch was opened to users in 2008 and is now fully operational, with 50 peer-reviewed projects already completed on the DESIRS FTS branch. The FTS coupled with the undulator source can simultaneously provide ultra-high spectral resolution (down to  $\delta\sigma = 0.08 \text{ cm}^{-1}$ ) and high SNR. We stressed that the measurement of absolute photoabsorption cross sections is not a straightforward procedure, especially in the windowless VUV spectral region. If we assume a sufficient instrumental resolution to not introduce significant error, the absolute cross section can be directly deduced from the Beer–Lambert law. Following the described methodology, absolute photoabsorption can be measured with an uncertainty below 5% ( $\sim 3\%$  under optimized experimental conditions). The main limitations are due to the jitter effect and the determination of the column density. We believe that some improvement could be achieved in both of these domains, and they are underway. Besides, new setups are being developed in order to produce transient species: a windowed and windowless DC discharge cell, a flow tube and a radio frequency cell, some of which are already available for the user community. The FTS efficiency should facilitate the measurement of absorption spectra from reactive species like radicals, ions or metastable species, that are known to be challenging to produce. Transient species data (oscillator strength, spectroscopy) are necessary due to their important role in atmospheric and interstellar medium modelling.

## Acknowledgements

A part of the FTS branch funding was supported by the ANR (Agence Nationale de la Recherche) under Grant No. 05-BLAN-0364. The authors thank Michel Vervloet for fruitful discussions on spectroscopic issues. We are also indebted to the general technical staff of Synchrotron SOLEIL for their support on the DESIRS beamline.

## References

- Aller, L. H. (1991). *Atoms, Stars, and Nebulae*. Cambridge University Press.
- Brown, L. R., Margolis, J. S., Norton, R. H. & Stedry, B. D. (1983). *Appl. Spectrosc.* **37**, 287–292.
- Chamberlain, J. (1979). *The Principles of Interferometric Spectroscopy*. New York: Wiley.
- Chan, W., Cooper, G. & Brion, C. (1991). *Phys. Rev. A*, **44**, 186–204.
- Cingöz, A., Yost, D. C., Allison, T. K., Ruehl, A., Fermann, M. E., Hartl, I. & Ye, J. (2012). *Nature (London)*, **482**, 68–71.

- Davis, S. P., Abrams, M. C. & Brault, J. W. (2001). *Fourier Transform Spectrometry*. San Diego: Academic Press.
- Eden, S., Limão-Vieira, P., Hoffmann, S. V. & Mason, N. J. (2006). *Chem. Phys.* **323**, 313–333.
- Eidelsberg, M., Lemaire, J. L., Federman, S. R., Stark, G., Heays, A. N., Sheffer, Y., Gavilan, L., Fillion, J.-H., Rostas, F., Lyons, J. R., Smith, P. L., de Oliveira, N., Joyeux, D., Roudjane, M. & Nahon, L. (2012). *Astron. Astrophys.* **543**, A69.
- Eidelsberg, M. & Rostas, F. (1990). *Astron. Astrophys.* **235**, 472–489.
- Forman, M. L., Steel, W. H. & Vanasse, G. A. (1966). *J. Opt. Soc. Am.* **56**, 59–63.
- Garcia, G. A., Cunha de Miranda, B. K., Tia, M., Daly, S. & Nahon, L. (2013). *Rev. Sci. Instrum.* **84**, 069902.
- Heays, A. N., Dickenson, G. D., Salumbides, E. J., de Oliveira, N., Joyeux, D., Nahon, L., Lewis, B. R. & Ubachs, W. (2011). *J. Chem. Phys.* **135**, 244301.
- Heays, A. N., Eidelsberg, M., Stark, G., Lemaire, J. L., Gavilan, L., Federman, S. R., Lewis, B. R., Lyons, J. R., de Oliveira, N. & Joyeux, D. (2014). *J. Chem. Phys.* **141**, 144311.
- Herzberg, G. & Spinks, J. W. T. (1950). *Molecular Spectra and Molecular Structure: Diatomic Molecules*. New York: Van Nostrand Reinhold.
- Hollenshead, J. & Klebanoff, L. (2006). *J. Vac. Sci. Technol. B*, **24**, 64–82.
- Hsieh, T.-F., Huang, L.-R., Chung, S.-C., Dann, T.-E., Tseng, P.-C., Chen, C. T. & Tsang, K.-L. (1998). *J. Synchrotron Rad.* **5**, 562–564.
- Hudson, R. D. & Carter, V. L. (1968). *J. Opt. Soc. Am.* **58**, 227–232.
- Jolly, A., Lemaire, J. L., Belle-Oudry, D., Edwards, S., Malmasson, D., Vient, A. & Rostas, F. (1997). *J. Phys. B*, **30**, 4315–4337.
- Kandula, D. Z., Gohle, C., Pinkert, T. J., Ubachs, W. & Eikema, K. S. E. (2010). *Phys. Rev. Lett.* **105**, 063001.
- Kauppinen, J., Kärkköinen, T. & Kyrö, E. (1978). *Appl. Opt.* **17**, 1587–1594.
- Keller-Rudek, H., Moortgat, G. K., Sander, R. & Sörensen, R. (2013). *Earth Syst. Sci. Data*, **5**, 365–373.
- Lerch, P., Dumas, P., Schilcher, T., Nadji, A., Luedeke, A., Hubert, N., Cassinari, L., Boege, M., Denard, J.-C., Stingelin, L., Nadolski, L., Garvey, T., Albert, S., Gough, Ch., Quack, M., Wambach, J., Dehler, M. & Filhol, J.-M. (2012). *J. Synchrotron Rad.* **19**, 1–9.
- Lewis, B. R., Gibson, S. T., Emami, M. & Carver, J. H. (1988). *J. Quant. Spectrosc. Radiat. Transfer*, **40**, 1–13.
- Lewis, B. R., Gibson, S. T., England, J. P., Stark, G. & West, J. B. (2002). *J. Chem. Phys.* **116**, 3286–3296.
- Lewis, B. R., Gibson, S. T., Morrill, J. S. & Ginter, M. L. (1999). *J. Chem. Phys.* **111**, 186.
- Lu, H.-C., Chen, H.-K., Chen, H.-F., Cheng, B.-M. & Ogilvie, J. F. (2010). *Astron. Astrophys.* **520**, A19.
- Marcouille, O., Brunelle, P., Chubar, O., Marteau, F., Massal, M., Nahon, L., Tavakoli, K., Veteran, J. & Filhol, J. M. (2007). *AIP Conf. Proc.* **879**, 311–314.
- Mercier, B., Compin, M., Prevost, C., Bellec, G., Thissen, R., Dutuit, O. & Nahon, L. (2000). *J. Vac. Sci. Technol. A*, **18**, 2533–2541.
- Nahon, L., Alcaraz, C., Marlats, J.-L., Lagarde, B., Polack, F., Thissen, R., Lepère, D. & Ito, K. (2001). *Rev. Sci. Instrum.* **72**, 1320.
- Nahon, L., de Oliveira, N., Garcia, G. A., Gil, J.-F., Joyeux, D., Lagarde, B. & Polack, F. (2013). *J. Phys. Conf. Ser.* **425**, 122004.
- Nahon, L., de Oliveira, N., Garcia, G. A., Gil, J.-F., Pilette, B., Marcouillé, O., Lagarde, B. & Polack, F. (2012). *J. Synchrotron Rad.* **19**, 508–520.
- Niu, M. L., Heays, A. N., Jones, S., Salumbides, E. J., van Dishoeck, E. F., De Oliveira, N., Nahon, L. & Ubachs, W. (2015). *J. Mol. Spectrosc.* **315**, 137–146.
- Niu, M. L., Salumbides, E. J., Zhao, D., de Oliveira, N., Joyeux, D., Nahon, L., Field, R. W. & Ubachs, W. (2013). *Mol. Phys.* **111**, 2163–2174.
- Oliveira, N. de, Joyeux, D., Phalippou, D., Rodier, J. C., Polack, F., Vervloet, M. & Nahon, L. (2009). *Rev. Sci. Instrum.* **80**, 043101.
- Oliveira, N. de, Roudjane, M., Joyeux, D., Phalippou, D., Rodier, J.-C. & Nahon, L. (2011). *Nat. Photon.* **5**, 149–153.
- Reichardt, G., Noll, T., Packe, I., Rotter, P., Schmidt, J.-S. & Gudat, W. (2001). *Nucl. Instrum. Methods Phys. Res. A*, **467–468**, 458–461.
- Roth, A. (2012). *Vacuum Technology*. Amsterdam: Elsevier.
- Rupper, P. & Merkt, F. (2004). *Rev. Sci. Instrum.* **75**, 613–622.
- Salumbides, E. J., Niu, M. L., Bagdonaite, J., de Oliveira, N., Joyeux, D., Nahon, L. & Ubachs, W. (2012). *Phys. Rev. A*, **86**, 022510.
- Seiler, R., Paul, T., Andrist, M. & Merkt, F. (2005). *Rev. Sci. Instrum.* **76**, 103103.
- Singh, P. J., Shastri, A., Sampath Kumar, R., Jha, S. N., Rao, S. V. N. B., D’Souza, R. & Jagatap, B. N. (2011). *Nucl. Instrum. Methods Phys. Res. A*, **634**, 113–119.
- Stark, G., Heays, A. N., Lyons, J. R., Smith, P. L., Eidelsberg, M., Federman, S. R., Lemaire, J. L., Gavilan, L., de Oliveira, N., Joyeux, D. & Nahon, L. (2014). *Astrophys. J.* **788**, 67.
- Stark, G., Lewis, B., Gibson, S. & England, J. (1999a). *Astrophys. J.* **520**, 732–736.
- Stark, G., Smith, P. L., Rufus, J., Thorne, A. P., Pickering, J. C. & Cox, G. (1999b). *J. Geophys. Res.* **104**, 16585–16590.
- Stark, G., Yoshino, K., Smith, P. L., Esmond, J. R., Ito, K. & Stevens, M. H. (1993). *Astrophys. J.* **410**, 837.
- Stark, G., Yoshino, K., Smith, P. L., Ito, K. & Parkinson, W. H. (1991). *Astrophys. J.* **369**, 574–580.
- Tang, X., Garcia, G. A., Gil, J.-F. & Nahon, L. (2015). *Rev. Sci. Instrum.* **86**, 123108.
- Trickl, T., Kung, A. & Lee, Y. (2007). *Phys. Rev. A*, **75**, 022501.
- Ubachs, W. (2005). *J. Electron Spectrosc. Relat. Phenom.* **144–147**, 97–101.
- Yao-Leclerc, I., Brochet, S., Chauvet, C., De Oliveira, N., Duval, J.-P., Gil, J.-F., Kubsy, S., Lagarde, B., Nahon, L., Nicolas, F., Silly, M., Sirotti, F. & Thomasset, M. (2011). *Proc. SPIE*, **8077**, 807712.
- Yoshino, K., Stark, G., Esmond, J. R., Smith, P. L., Ito, K. & Matsui, T. (1995). *Astrophys. J.* **438**, 1013.